

Ultra-high performance microwave spectral filters using optical microcombs

David J. Moss

Optical Sciences Centre, Swinburne University of Technology, Hawthorn, VIC 3122, Australia

dmoss@swin.edu.au

Keywords: Microwave photonic filters, optical microcombs, integrated optics.

Abstract

Microwave photonic (MWP) filters are essential components in microwave systems due to their wide bandwidth, low loss, and immunity to electromagnetic interference. A sharp transition band is critical for precise spectral shaping and interference suppression, yet conventional MWP filters face challenges in achieving both sharp transitions and high reconfigurability. Adaptive MWP filters with sharp transition based on a transversal filter structure using an optical microcomb source are demonstrated in this paper. Four different types of single-band MWP filters with roll-off rates up to ~ 32.6 dB/GHz and a minimum shape factor of ~ 1.15 are achieved. In addition, simply through designing tap coefficients, band-pass filters with tunable centre frequencies ranging from 5 GHz to 15 GHz and dual-band MWP filters with various filter response are demonstrated without changing any hardware, where sharp transition is also validated. The adaptive filters with sharp transition presented in this paper offer a stable and highly reconfigurable solution for applications requiring stringent spectral selectivity, such as next-generation wireless networks, high-resolution radar imaging, and advanced biomedical photonic sensing.

1. Introduction

Microwave photonic (MWP) filters have emerged as a crucial technology in modern communication systems, radar, and high-speed signal processing due to their ability to process signals with wide bandwidth, low loss, and immunity to electromagnetic interference [1, 2]. These advantages make MWP filters a superior alternative to traditional electronic filters. It is critical to achieve MWP filters with sharp transitions, since it facilitates precise spectral shaping and enhanced suppression of out-of-band interference, thereby improving the accuracy of desired signal extraction [3].

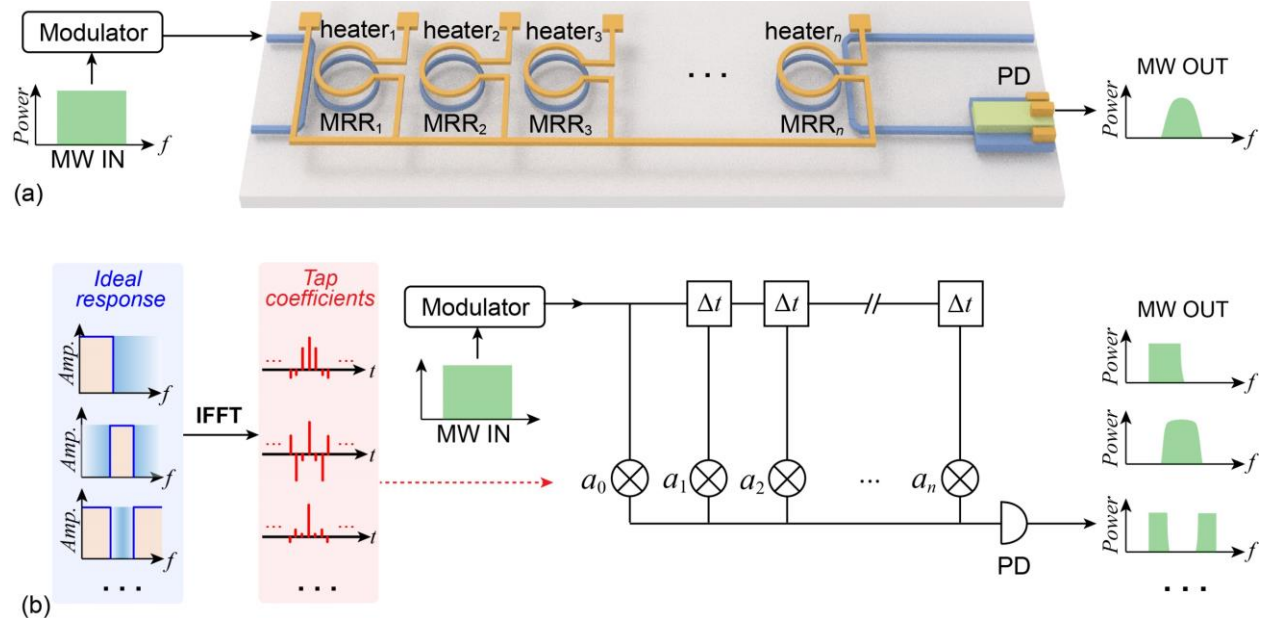


Figure 1. Schematic of microwave photonic (MWP) filters with high roll-off performance. (a) Schematic of an infinite impulse response (IIR) MWP filter based on cascaded microring resonators (MRRs). MW: microwave. PD: photodetector. (b) Schematic of an FIR filter based on the transversal filter structure with high reconfigurability. IFFT: inverse fast Fourier transform.

Conventional MWP filters often face inherent challenges in simultaneously achieving high roll-off performance, high reconfigurability, and broad tuning bandwidth. MWP filters can be categorized into infinite impulse response (IIR) MWP filters and finite impulse response (FIR) MWP filters [4]. IIR MWP filters are typically implemented using optical resonators [5-9], optical

delay lines [10], optical-electrical feedback loops [11], ring-assisted Mach-Zehnder Interferometers (MZIs) [12, 13], or stimulated Brillouin scattering in waveguides [14, 15], which allow for the realization of high-quality factor filtering responses, enabling sharp roll-off characteristics. While IIR MWP filters exhibit superior spectral selectivity, they are with low reconfigurability and suffer from instability as well as sensitivity to fabrication imperfections [6]. One of the approaches to achieving high roll-off performance in MWP filters is the use of cascaded microresonators (**Figure 1(a)**). Multiple coupled resonators with high quality factors are cascaded to achieve sharp filtering responses, which introduces significant design and fabrication challenges [9]. The resonance characteristics of each microresonator must be precisely controlled, and thermal variations as well as fabrication-induced resonance mismatches can easily degrade filter performance.

FIR MWP filters, typically implemented via transversal filter structures (**Figure 1(b)**) [16-19], offer high flexibility and stability due to their inherent non-recursive nature. They use a finite number of discrete taps to perform weighted summation, allowing easy reconfiguration. However, a limitation of FIR MWP filters is their relatively slow roll-off rate, as achieving sharp spectral transitions requires a large number of taps, which can be difficult to implement in traditional configurations based on discrete laser arrays [32] and fibre Bragg gratings (FBGs) [3].

Recently, optical microcombs [20-22], which are optical frequency combs generated by micro-scale resonators, offer distinct advantages for FIR MWP filters, as they can provide a larger number of discrete wavelengths while also having a compact device footprint [23-25]. This makes them an ideal candidate for realizing MWP filters with enhanced roll-off characteristics. Each comb line serves as an independent tap in the transversal filter structure, and the amplitude of each tap can be designed to enable filter responses with steep roll-off performance. Unlike IIR MWP filters,

which rely on feedback loops and resonators, the microcomb-based approach does not suffer from inherent stability or sensitivity to fabrication imperfections. Another key advantage of the microcomb-based MWP filters is the high reconfigurability. The filter shape can be modified simply by designing different tap coefficients to adapt to different filtering requirements without changing any hardware.

In this paper, we demonstrate ultrahigh-performance adaptive MWP filters based on an optical microcomb source. We achieve four single-band filters with different filter shapes, which have extremely sharp roll-off performance with roll-off rates up to ~ 32.6 GHz and a minimum 20-dB shape factor of ~ 1.15 . To describe the tunability of the filters, band-pass filters with tunable centre frequencies ranging from 5 GHz – 15 GHz are demonstrated. In addition, we present dual-band filters with various filter response by using the same configuration to verify the reconfigurability, where high roll-off performance is also validated. The ultrahigh-performance adaptive filters presented in this paper open new avenues for the application of MWP filters in systems requiring high spectral selectivity, such as wireless communication, radar, and biomedical imaging systems, where sharp roll-off performance and different filter response are necessary.

2. Principle

Figure 2(a) shows the schematic diagram of an ultrahigh-performance MWP filter based on a soliton crystal microcomb. The soliton crystal microcomb is generated by an integrated microring resonator (MRR) and the schematic of microcomb generation is shown in **Figure 2(b)**. The MRR is pumped by a continuous-wave (CW) laser, which is amplified by an erbium-doped fibre amplifier (EDFA). A polarization controller is used to adjust the polarization, optimizing the power coupled to the MRR. When the pump laser is precisely tuned, it transitions from a blue-detuned to a red-detuned regime, which leads to the generation of the soliton crystal microcomb with a free

spectral range (FSR) of \sim 49 GHz. The generated microcomb, which serves as a multi-wavelength optical source, is fed into an intensity modulator (IM), yielding replicas of the input microwave signal. Then the modulated optical signal goes through a spool of single-mode fibre (SMF), where a time delay between adjacent wavelength channels Δt in **Figure 1** is introduced. Next, the delayed signal is shaped by a Waveshaper to achieve the desired tap coefficients. The calculated tap coefficients of low-pass, band-pass, high-pass, and band-stop filters are shown in **Figure 2(c)**. Instead of employing equal tap coefficients to realize low-pass filters and with additional modifications to shape the filter response in our previous work [18, 26], we directly design the tap coefficients by applying inverse fast Fourier transform (IFFT) to the ideal filters' radio-frequency (RF) amplitude response. This approach enables improved roll-off performance by ensuring that the obtained filter shapes more accurately align with the ideal response. Finally, the delayed and weighted taps are summed upon photodetection and converted to microwave signals at the output. A vector network analyzer (VNA) is used to measure the RF response of the system. **Figure 2(d)** shows the simulated RF amplitude response of low-pass, band-pass, high-pass, and band-stop filters.

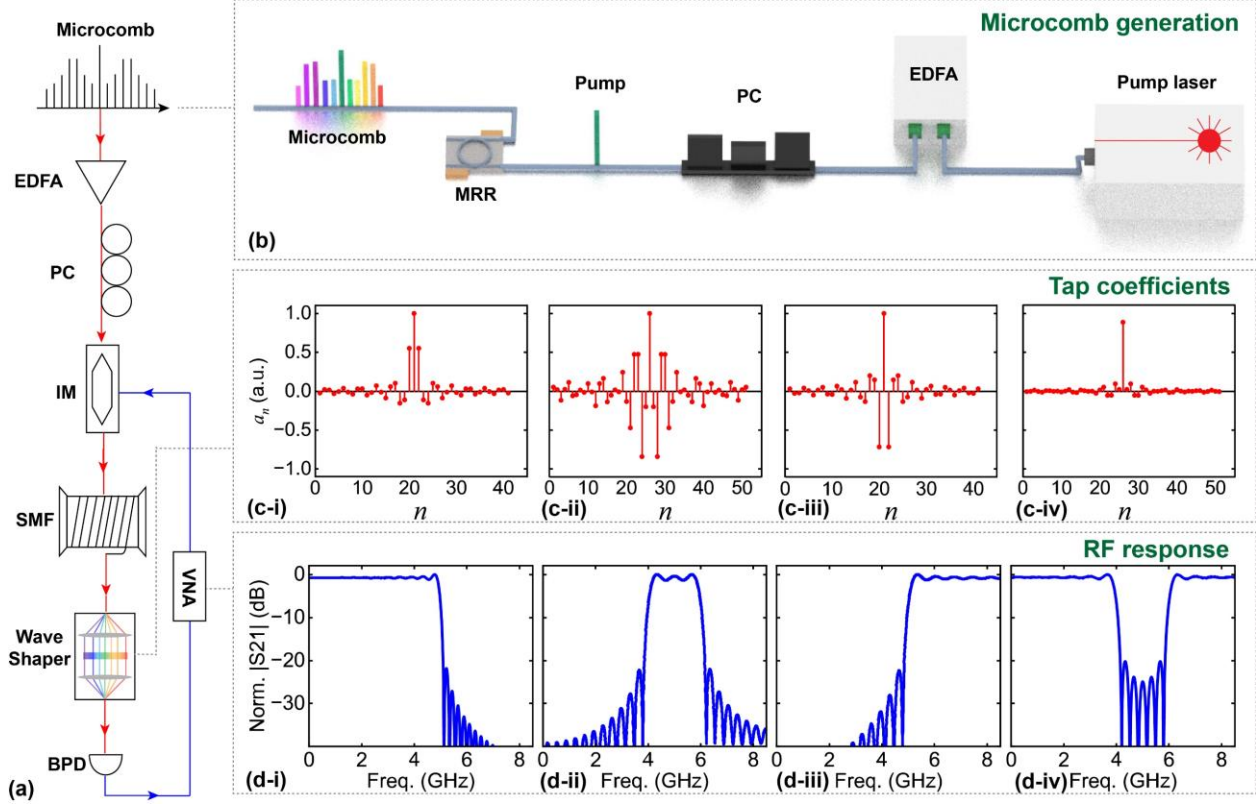


Figure 2. Schematic configuration of ultrahigh-performance adaptive MWP filters. (a) Schematic of an ultrahigh-performance microwave photonic (MWP) filter based on a soliton crystal microcomb. EDFA: erbium-doped fibre amplifier. PC: polarization controller. IM: Intensity modulator. SMF: single-mode fibre. BPD: balanced photo detector. VNA: vector network analyzer. (b) Schematic of soliton crystal microcomb generation. MRR: microring resonator. (c) Calculated tap coefficients of (i) low-pass filter, (ii) band-pass filter, (iii) high-pass filter, and (iv) band-stop filter. (d) Simulated RF amplitude response of (i) low-pass filter, (ii) band-pass filter, (iii) high-pass filter, and (iv) band-stop filter.

The transfer function of the MWP transversal filter system in **Figure 2(a)** can be described as [27]

$$H(\omega) = \sum_{n=0}^{M-1} a_n e^{-j\omega n \Delta t}, \quad (1)$$

where M is the number of taps, a_n ($n = 0, 1, 2, \dots, M - 1$) is the tap coefficient of the n^{th} tap, and ω is the angular frequency of the input microwave signal. By designing a_n ($n = 0, 1, 2, \dots, M - 1$), different filter shapes can be achieved without changing the hardware. The time delay Δt is

determined by the FSR of microcomb $\Delta\lambda$ and the dispersion of the SMF, which can be further expressed as [20]

$$\Delta t = \Delta\lambda \times L \times D_2, \quad (2)$$

where L is the fibre length and D_2 is the second-order dispersion (SOD) parameter of the dispersive module. As MWP transversal filters have a finite impulse response, they exhibit a periodic spectral response, and the FSR can be calculated by $FSR_{MW} = 1/\Delta t$. The operation bandwidth (*i.e.*, the Nyquist frequency) is half of FSR_{MW} , which can be expressed as [20]

$$OB = \frac{1}{2 \Delta t}. \quad (3)$$

The roll-off rate and shape factor are two important metrics to demonstrate the roll-off performance of MWP filters. The roll-off rate (*ROR*) quantifies how rapidly the filters transition from passbands to stopbands, which can be described as [19]

$$ROR = \frac{A}{|f_{-3dB} - f_{ref}|}, \quad (4)$$

where A is the attenuation from the -3 dB point in the transition band to a reference point, and f_{3dB} and f_{ref} are the frequencies at -3 dB point and the reference point, respectively. A higher roll-off rate indicates better stop-band suppression and less interference. The shape factor (*SF*) describes filters' spectral selectivity and is defined as the ratio of bandwidth at a reference level to the bandwidth at the -3dB level. The shape factor is given by [7]

$$SF = BW_{ref} / BW_{-3dB}, \quad (5)$$

where BW_{ref} and $BW_{-3\text{dB}}$ are the bandwidth at a reference level and -3 dB level, respectively. A smaller shape factor (closer to 1) indicates a sharper transition and better spectral selectivity.

3. Experimental demonstration

3.1 Soliton crystal microcomb

Soliton crystal microcomb represents a unique and robust class of optical frequency comb, operating in a highly coherent state that is enabled by optical parametric oscillation within an integrated MRR. The MRR used here is fabricated on a complementary metal-oxide-semiconductor (CMOS)-compatible doped silica glass platform [28, 29], with a quality (Q) factor of approximately 1.9 million (**Section S1**, Supporting Information) and a radius of $\sim 592 \mu\text{m}$ as shown in **Figure 3(a)**, yielding a FSR of $\sim 49 \text{ GHz}$ (or $\sim 0.4 \text{ nm}$). This narrow FSR results in a large number of available wavelengths in the telecommunications C-band.

The soliton crystal microcomb is characterized by deterministic formation, facilitated by mode-crossing-induced background waves and the Kerr nonlinearity, combined with high intracavity power [30]. The soliton crystal microcomb is generated by using avoided mode crossing (AMX), which is shown in **Figure 3(b)** and obtained by employing the setup described in **Section S1** (Supporting Information) [31]. Unlike dissipative Kerr solitons (DKS), soliton crystal microcomb exhibits minimal intracavity energy variation during its generation, thereby eliminating the need for complex tuning techniques. The initiation of the soliton crystal microcomb is achieved via a simple pump wavelength sweeping method [32], where a CW pump laser (Yenista Optics), amplified to 32.1 dBm by an EDFA (IdealPhotonics), is manually swept in wavelength from blue to red until modulation instability oscillations emerge. With the detuning between the pump and the MRR's resonance slipping farther, a stable soliton crystal oscillation state is achieved,

generating over 90 wavelength channels across the C band at a pump wavelength of 1551.3 nm, as shown in **Figure 3(c)**. As can be seen, the soliton crystal microcomb exhibits scalloped-shaped spectra that, although it has been regarded as a potential limitation for practical applications, has in fact been shown not to present a significant drawback. This is partly attributed to the higher power conversion efficiency of soliton crystal microcombs compared with single soliton states [20]. In addition, the soliton crystal microcomb demonstrated remarkable long-term power stability, with a measured relative standard deviation of -14 dB over 66 hours [33], confirming its suitability for advanced photonic signal processing applications.

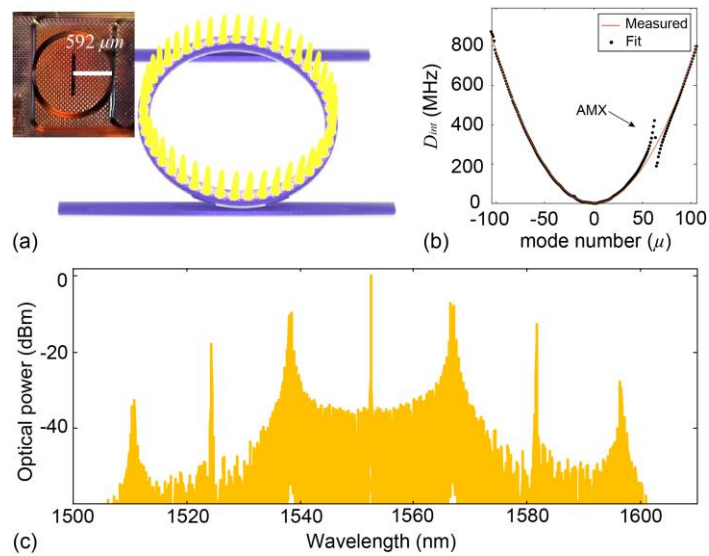


Figure 3. Soliton crystal microcomb. (a) Schematic representation and the image (upper inset) of the integrated MRR. (b) Measured integrated dispersion D_{int} of the integrated MRR showing an avoided mode crossing (AMX) location of ~ 1580.2 nm. (c) Optical spectrum of the generated soliton crystal microcomb with a free spectral range (FSR) of ~ 49 GHz.

3.2 Ultrahigh-performance adaptive MWP filters

The MWP filters with sharp roll-off performance and diverse filter shapes were experimentally demonstrated. The input microwave signal was modulated onto the generated microcomb (**Figure 3(c)**) yielding microwave replicas. Then the modulated optical signal went through a spool of SMF

with a length L of ~ 8.2 km to provide the time delay Δt . The SOD parameter D_2 of the SMF was ~ 17.4 ps nm $^{-1}$ km $^{-1}$, which corresponded to a Δt of ~ 56.5 ps and an operation bandwidth OB of ~ 8.84 GHz according to **Equation (3)**. To achieve desired tap coefficients a_n ($n = 0, 1, 2, \dots, M - 1$), the signal was shaped in power via a Waveshaper (Finisar). The Waveshaper also separated the wavelength channels into two categories according to the sign of tap coefficients. The signals were then directed to the two ports of a balanced photodetector (Finisar), where the weighted and delayed taps were summed upon photodetection, and positive as well as negative taps were enabled.

To demonstrate the sharp roll-off performance of the MWP filters, we implemented low-pass and high-pass filters with cut-off frequencies f_{ct} of 5 GHz, as well as band-pass and band-stop filters with centre frequencies f_c of 5 GHz and a pass/stop band of 2 GHz. The calculated tap coefficients and simulated RF amplitude response are shown in **Figures 2(c) and (d)**, respectively.

Figure 4(a) shows the designed tap coefficients and the measured optical spectra of the shaped microcomb, measured using an optical spectrum analyzer (OSA, Anritsu), for the four different types of MWP filters. Further details on the tap number for proposed MWP filters are discussed in **Section S2** (Supporting Information). A close agreement between the designed tap coefficients (green circles for positive tap coefficients and yellow circles for negative tap coefficients) and the power of the measured microcomb lines (green solid lines for positive tap coefficients and yellow solid lines for negative tap coefficients) was obtained, indicating that the microcomb lines were accurately shaped.

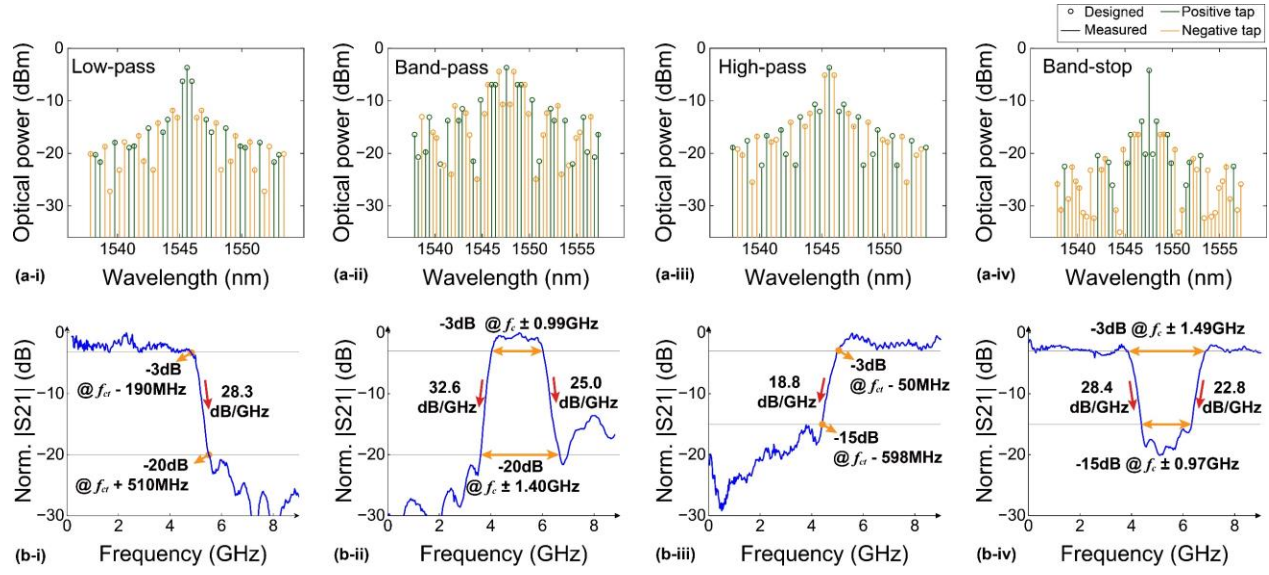


Figure 4. Experimental demonstration of MWP filters. (a) Designed tap coefficients (circles) and optical spectra of shaped microcomb (solid lines) for (i) low-pass filter, (ii) band-pass filter, (iii) high-pass filter, and (iv) band-stop filter. Green circles and solid lines for positive tap coefficients and yellow circles and solid lines for negative tap coefficients. (b) Measured RF amplitude response of (i) a low-pass filter with a roll-off rate of ~ 28.3 GHz and a 20-dB shape factor of ~ 1.15 , (ii) a band-pass filter with a roll-off rate of ~ 32.6 GHz for low-frequency edge as well as ~ 25.0 GHz for high-frequency edge and a 20-dB shape factor of ~ 1.55 , (iii) a high-pass filter with a roll-off rate of ~ 18.8 GHz and a 15-dB shape factor of ~ 1.17 , and (iv) a band-stop filter with a roll-off rate of ~ 28.4 GHz for low-frequency edge as well as ~ 22.8 GHz for high-frequency edge and a 15-dB shape factor of ~ 1.53 .

We measured the RF amplitude response of the filters by a VNA (Anritsu) as shown in **Figure 4(b)**. The low-pass filter exhibited a high roll-off rate of ~ 28.3 dB/GHz with a reference point f_{ref} in **Equation (4)** at -20 dB. The roll-off rates of the band-pass filter [ROR_l, ROR_h], where ROR_l and ROR_h are defined as the roll-off rates for low- and high-frequency edges, were $\sim [32.6, 25.0]$ dB/GHz at $f_{ref} = -20$ dB. For the high-pass filter, the roll-off rate was ~ 18.8 dB/GHz at $f_{ref} = -15$ dB. The band-stop filter exhibited roll-off rates of $\sim [28.4, 22.8]$ dB/GHz at $f_{ref} = -15$ dB. The $BW_{3\text{dB}}$ and $BW_{-20\text{dB}}$ of the low-pass filter (**Figure 4(b-i)**) were $f_{ct} - 190$ MHz and $f_{ct} + 510$ MHz, respectively, corresponding to a 20 dB shape factor of ~ 1.15 . The shape factors of the band-pass, high-pass, and band-stop filters (**Fig. 4(b-ii)–(b-iv)**) were ~ 1.55 , ~ 1.17 , and ~ 1.53 , respectively.

The results demonstrate that the proposed filters have achieved a sharp roll-off performance. In our previous work [26, 34], low-pass filters were initially realized with equal tap coefficients, followed by refinement of the tap coefficients to tailor the filter response. Instead of employing this method, we directly obtained the tap coefficients by applying IFFT to the ideal RF amplitude response here. Compared to our previous work [26, 34], this method ensured that the system response more closely aligned with the ideal response, which significantly improved the roll-off rate from 5.2 dB/GHz to 32.6 dB/GHz, achieving a shape factor of ~ 1.15 . The sharp roll-off performance is essential for improving signal selectivity and mitigating spectral leakage from adjacent channels in microwave signal processing and data transmission systems. Since the soliton crystal microcomb provided enough number of taps (**Section S2**, Supporting Information), the roll-off performance of the proposed MWP filters was mainly limited by the experimentally induced processing errors, including noise of the soliton crystal microcomb, chirp and uneven response of the IM, high-order dispersion in SMF, shaping errors of the Waveshaper, and noise of the BPD [35]. In our experiments, we employed a two-stage feedback control method (see **Section S3**, Supporting Information) to calibrate the tap coefficients [36], which mitigated the errors resulting from static and slowly varying error sources [37]. Residual errors remained in the system that could not be compensated for via the implemented two-stage feedback control method. These were mainly fast varying errors, such as the amplitude and phase distortions induced by the microcomb and BPD.

To demonstrate the tunability of the MWP filters, the tap coefficients were designed to achieve band-pass filters with different centre frequencies f_c . Here we employed a spool of SMF with a fibre length of ~ 5.1 km, corresponding to an operation bandwidth OB of ~ 28.7 GHz. We note that

the maximum *OB* is limited by half of the FSR of the soliton crystal microcomb. When the operation is beyond half of the FSR (~ 24.5 GHz), strong crosstalk between adjacent taps occurs.

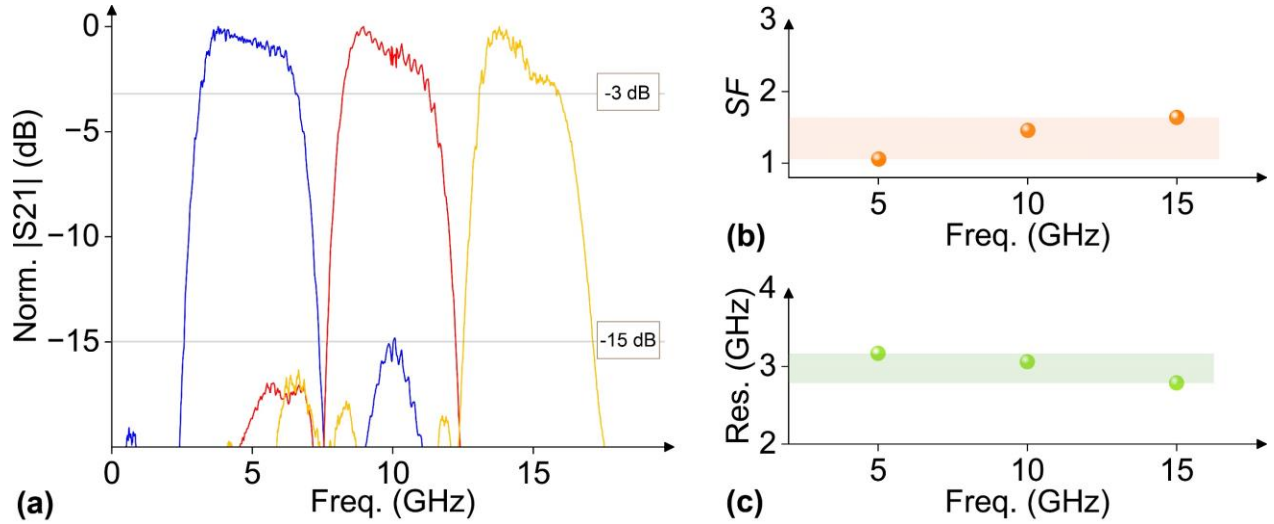


Figure 5. Tunability of MWP band-pass filters. (a) Measured RF amplitude response of tunable band-pass filters with centre frequencies of 5 GHz, 10 GHz, and 15 GHz. (b) Features of the tunable band-pass filters' shape factors. (c) Features of the tunable band-pass filters' resolution.

As shown in **Figure 5(a)**, three band-pass filters have been realized, each with a 3-GHz passband bandwidth and tunable centre frequencies ranging from 5 GHz to 15 GHz. The roll-off rates were $\sim[17.2, 16.1]$ dB/GHz, $\sim[21.4, 14.3]$ dB/GHz, and $\sim[21.0, 12.9]$ dB/GHz for the three band-pass filters with centre frequencies at 5 GHz, 10 GHz, and 15 GHz, respectively. With the tuning of the centre frequencies, the filters showed consistent low shape factors ranging from ~ 1.06 to ~ 1.64 , as can be seen from **Figure 5(b)**. This consistency suggests that the proposed MWP filters keep a sharp transition band without being affected by the centre frequency, which is highly beneficial for applications requiring uniform filter performance across a wide bandwidth. The resolution (3-dB bandwidth) of the filters also remained consistent (**Figure 5(c)**) with a deviation under 210 MHz. The combination of sharp roll-off and tunable centre frequency while maintaining stable resolution reflects that the proposed MWP filter system is well-calibrated and precisely controlled.

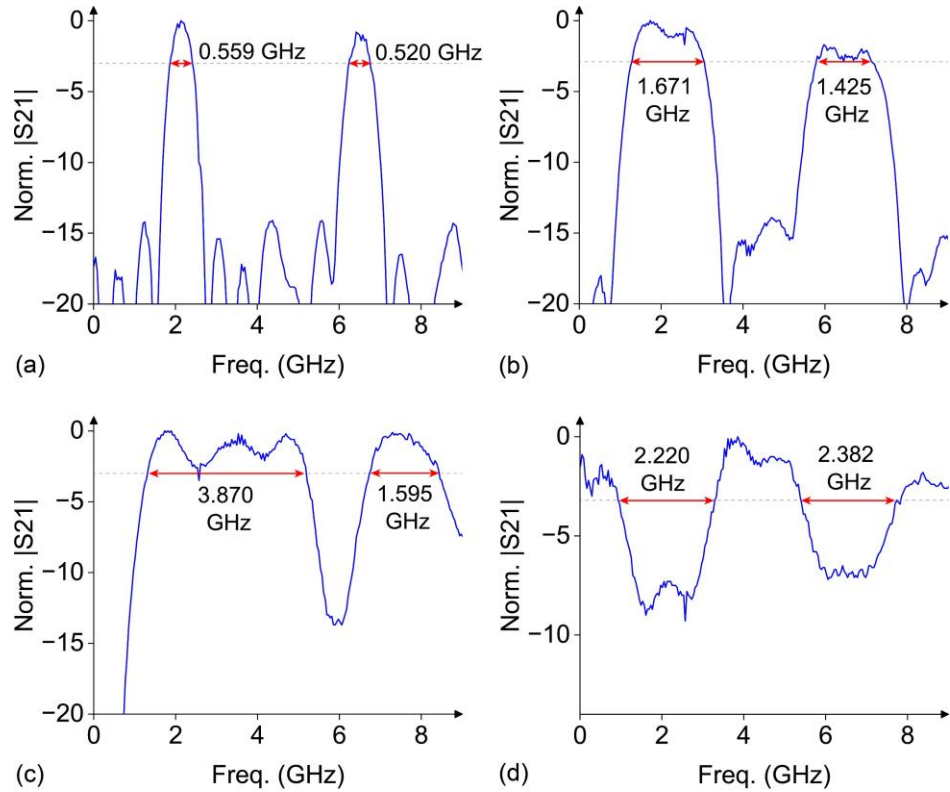


Figure 6. Dual-band MWP filters. Measured RF amplitude response of three dual passband filters and one dual stopband filter, including two dual passband filters with equal passband bandwidth, one with (a) 0.5 GHz and the other with (b) 1.5 GHz, (c) one dual passband filter with passband bandwidth of 4 GHz and 1.5 GHz, and (d) a dual stopband filter with two stopbands each having a bandwidth of 2 GHz.

Dual-band microwave filters have also attracted great interest because of the growing demand for multifunctional microwave systems supporting various modern applications [38-40]. Four distinct dual-band MWP filters were demonstrated here (Figure 6), further verifying the reconfigurability of the MWP filters. An 8.2-km SMF was employed, resulting in an operational bandwidth of \sim 8.84 GHz. Tap coefficients were designed to achieve three dual passband filters and one dual stopband filter, including two dual passband filters with equal passband bandwidth – one with 0.5 GHz (Figure 6(a)) and the other with 1.5 GHz (Figure 6(b)), one dual passband filter with passband bandwidth of 4 GHz and 1.5 GHz (Figure 6(c)), and a dual stopband filter with two stopbands each having a bandwidth of 2 GHz (Figure 6(d)).

Figure 6 shows the RF amplitude response of the four filters. The roll-off rates of these filters were measured to be $\sim[10.7, 10.3, 20.0, 21.9]$ dB/GHz, $\sim[19.1, 20.2, 16.9, 9.3]$ dB/GHz, $\sim[12.8, 13.7, 10.1, 9.7]$ dB/GHz, and $\sim[9.9, 9.3, 7.2, 5.3]$ dB/GHz, respectively. The results show that dual-band MWP filters with various filter shapes can be achieved, verifying the high reconfigurability and consistent sharp roll-off performance of the proposed MWP filter.

To comprehensively examine the performance of MWP filters, RF metrics including spurious-free dynamic range (SFDR), RF link gain, and noise figure are adopted to characterize the RF performance of the system. To characterize the linearization of the proposed filter, we assessed the SFDR of a low-pass filter by using the two-tone method (**Figure 7(a)**) [41]. The RF response of the low-pass filter is shown in **Figure 7(b)** with a cut-off frequency of ~ 5 GHz. A two-tone test [14] at the frequency of 1 GHz was performed, where two CW RF signals at 1 GHz and 1.01 GHz were generated by an arbitrary waveform generator (AWG, Keysight) and then simultaneously fed to the IM with the same power. Through varying the RF input power of the two-tone signal from -5.66 dBm to -0.43 dBm and monitoring the output signals from the BPD on the electrical spectrum analyzer (ESA, Keysight), the amplitude of the third-order intermodulation distortion (IMD3) at 0.99 GHz and 1.02 GHz was recorded (**Figure 7(c)**), indicating a SFDR of ~ 91 dB·Hz $^{2/3}$ as shown in **Figure 7(d)**.

RF link gain of filter passbands reflects the overall signal transfer efficiency from the input to the output. The RF link gain at frequency f can be described as [2]

$$G(f) = 10\log_{10}(P_{out} / P_{in}) \quad (6)$$

where P_{out} and P_{in} are the RF output and input power, respectively. The RF link gain of the proposed low-pass MWP filter (**Figure 7(b)**) was ~ -14.8 dB measured at 1 GHz, where the main sources of

degradation are inefficient optical to electrical and electrical to optical conversion [42] as well as optical losses [2]. The optical losses can be compensated for by employing low-noise components and optical amplifiers. Noise figure quantifies the degradation of signal-to-noise ratio induced by system-inherent noise, which can be expressed by [2]

$$NF = 10\log_{10}(SNR_{in} / SNR_{out}) \quad (7)$$

where SNR_{in} and SNR_{out} are the signal-to-noise ratio (SNR) of the input and output signals, respectively, with an assumption that only the thermal noise exists at the input. The noise figure of the low-pass filter in **Figure 7(b)** was ~ 19.7 dB, depending on the noise of the soliton crystal microcomb, optical and RF amplifiers, and BPD.

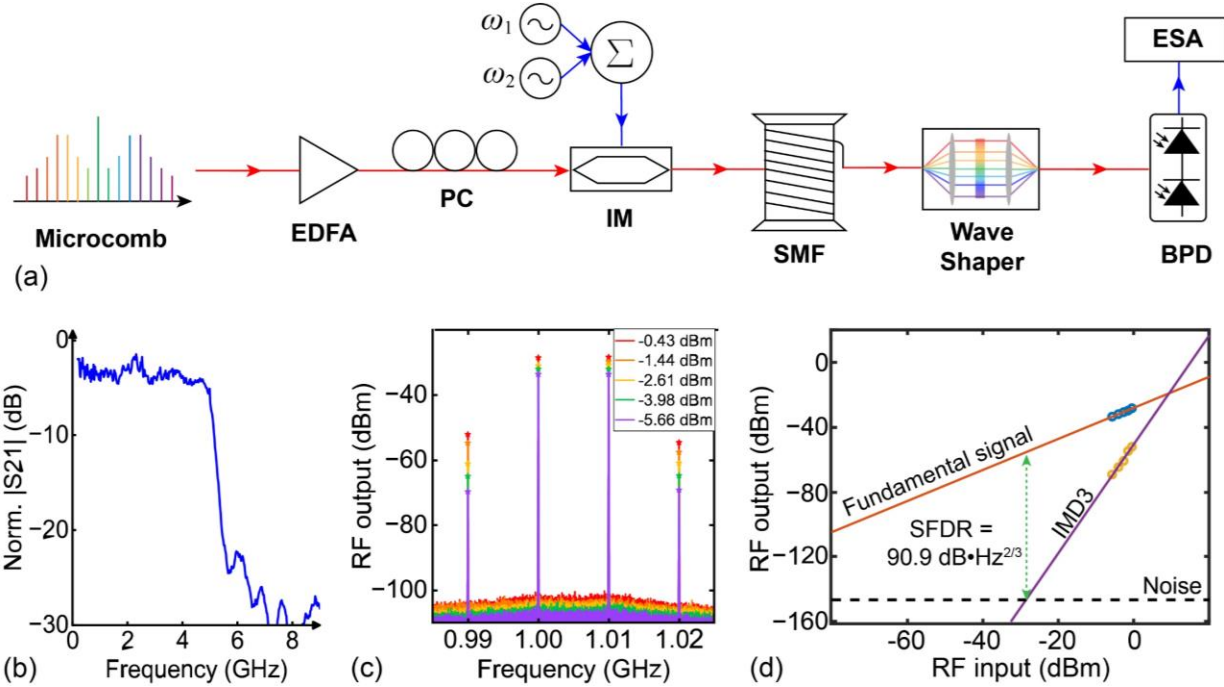


Figure 7. Linearization of the MWP filters. (a) Schematic of the experimental setup to demonstrate the linearization of the MWP filters. ESA: electrical spectrum analyzer. ω_1 and ω_2 : angular frequencies of the two-tone input RF signal. (b) RF amplitude response of the proposed low-pass filter, with a cut-off frequency of ~ 5 GHz. (c) Measured two-tone RF output spectra at different input RF power. (d) Measured spurious-free dynamic range (SFDR) of the low-pass MWP filter. IMD3: third-order intermodulation distortion.

Table 1 gives a summary of state-of-the-art MWP filters. For IIR MWP filters achieved by direct response mapping (DRM), although they feature simple structures and a high degree of integration, their roll-off performance largely depends on the sharpness of the employed optical filters. To address this limitation, cascaded MRRs have been introduced to achieve sharper optical filtering responses and thus enhance the roll-off performance of MWP filters after the conversion of phase modulation to intensity modulation (PM-IM) [7, 9]. FBGs have also been exploited after optical filters to attenuate phase modulated sidebands [3]. Although this led to enhanced shaped factors, the improvement sacrificed the reconfigurability of MWP filters due to the fixed spectral characteristics of FBGs. IIR MWP filters based on SBS in on-chip waveguides [43] or optical fibre [44] can achieve sharp transitions between the passband and stopband because of the narrow linewidth of the Brillouin gain spectrum, typically around tens of MHz [45]. However, this narrow linewidth constrains the tunability of the filter bandwidth [46].

In this work, we achieve FIR MWP filters based on the transversal filter system using a soliton crystal microcomb source, offering an ultrahigh roll-off performance and highly reconfigurable solution. By applying different tap coefficients and time delays, the system can synthesize arbitrary RF filter responses. We demonstrate four different types of single-band MWP filters as well as dual-band filters with various filter response, where both the bandwidth and centre frequency of the filters are tunable. In contrast to the approach adopted in our previous work [26, 34, 35], where equal tap coefficients were employed to realize low-pass filters first followed by additional modifications to tailor the filter response, we directly calculate the tap coefficients by applying IFFT to the desired RF amplitude response. This method facilitates improved roll-off performance, achieving a shape factor of ~ 1.15 , by ensuring the system response more accurately aligns with the ideal response.

Table 1. Comparison of state-of-the-art MWP filters. SFDR: spurious free dynamic range. ROR: roll-off rate. DRM: direct response mapping. MRR: microring resonator. RAMZI: ring-assisted Mach-Zehnder Interferometer. DFBR: distributed feedback resonator. TOBF: tunable optical band-pass filter. FBG: fibre Bragg grating. EPS-FBG: equivalent phase-shifted FBG. SBS: simulated Brillouin scattering. PM-IM: phase modulation to intensity modulation. TFS: transversal filter structure. A: low-pass filter. B: band-pass filter. C: high-pass filter. D: band-stop filter. E: dual passband filter. F: dual stopband filter.

Mechanism	Structure	Number of functions	Type of functions	Tuning range (GHz)	SFDR (dB·Hz ^{2/3})	ROR (dB/GHz)	Shape factor
DRM ^[7]	Two cascaded MRRs	1	B	4.0 – 21.5	–	–	1.23
DRM ^[9]	Four cascaded MRRs	1	B	4.0 – 36.0	–	10.23	–
DRM ^[47]	RAMZI	1	A	0 – 6.0	81.4	–	–
DRM ^[6]	DFBR waveguide Bragg grating	1	B	10.0 – 67.5	95.8	7.0	–
DRM ^[3]	TOBF + FBGs	1	B	6.3 – 22.4	–	–	1.88
DRM ^[40]	EPS-FBG	1	E	0.8 – 7.4	89.8	–	3.3
SBS ^[43]	Waveguide	1	D	5.0 – 20.0	92.2	–	–
SBS ^[44]	Optical fibre	2	B, E	1.65 – 2.15	–	–	1.35
TFS ^[26]	Microcomb	4	A, B, C, D	2.0 – 6.0	–	–	–
TFS ^[34]	Microcomb	1	B	3.28 – 19.4	–	5.2	–
This work	Microcomb	6	A, B, C, D, E, F	0 – 25.0	90.9	32.6	1.15

The roll-off performance is theoretically programmable but practically limited by the number of taps and the experimentally induced processing errors, including noise of the soliton crystal microcomb, chirp and uneven response of the IM, high-order dispersion in SMF, shaping errors of the Waveshaper, and noise of the BPD [35]. By reducing the linewidths and noise of lasers for pumping microcombs, using dispersive devices without high-order dispersion such as Bragg gratings, and employing advanced feedback control methods, there is still room for future

improvement of the roll-off performance. The present low-pass MWP filter is with a SFDR of ~ 91 $\text{dB}\cdot\text{Hz}^{2/3}$, which is comparable to those reported in other works. To increase the SFDR, an SBS assisted filter can be incorporated for carrier suppression [40].

These results confirm the effectiveness of optical microcombs in forming the basis for transversal filter microwave spectral filters [48 – 128] potentially involving advanced circuit designs [129 – 136] including graphene oxide and other 2D material based devices, [137 – 174] with applications to quantum optics. [175 – 190]

4. Conclusions

In this paper, we proposed ultrahigh-performance adaptive MWP filters based on a soliton crystal microcomb source. We demonstrated four single-band filters with distinct filter response, achieving extremely sharp roll-off rates up to ~ 32.6 GHz and a minimum 20-dB shape factor of ~ 1.15 . To describe the tunability of the filters, band-pass filters with tunable centre frequencies ranging from 5GHz – 15 GHz were realized. In addition, we implemented dual-band filters with different filter shapes by using the same configuration, validating their high reconfigurability while maintaining high roll-off performance. The ultrahigh-performance adaptive filters presented in this paper offer a promising solution for the applications demanding high spectral selectivity and reconfigurability.

Conflict of interests

The authors declare no conflict of interests.

References

[1] J. Yao, “Microwave Photonic Systems,” *Journal of Lightwave Technology*, vol. 40, no. 20, pp. 6595-6607, 2022.

- [2] Y. Liu *et al.*, "Integrated microwave photonic filters," *Adv. Opt. Photon.*, vol. 12, no. 2, pp. 485-555, 2020.
- [3] Q. Zhang *et al.*, "A single passband microwave photonic filter with enhanced flat top and shape factor based on tunable optical bandpass filter and fiber Bragg gratings," *Optics & Laser Technology*, vol. 168, pp. 109838, 2024.
- [4] J. Capmany *et al.*, "A Tutorial on Microwave Photonic Filters," *Journal of Lightwave Technology*, vol. 24, no. 1, pp. 201, 2006.
- [5] L. Xu *et al.*, "Silicon-on-insulator-based microwave photonic filter with widely adjustable bandwidth," *Photonics Res.*, vol. 7, no. 2, pp. 110-115, 2019.
- [6] C. Porzi *et al.*, "Silicon-on-Insulator Microwave Photonic Filter With Widely Tunable and Reconfigurable Flat-Top Bandpass Functionality," *Journal of Lightwave Technology*, vol. 40, no. 20, pp. 6666-6675, 2022.
- [7] W. Cheng *et al.*, "Tunable bandpass microwave photonic filter with largely reconfigurable bandwidth and steep shape factor based on cascaded silicon nitride micro-ring resonators," *Opt. Express*, vol. 31, no. 16, pp. 25648-25661, 2023.
- [8] L. Liu *et al.*, "Ultra-High Peak Rejection, Sub-Gigahertz Narrowband and Bandwidth Tunable Microwave Photonic Filter Based on Silicon Racetrack Resonators," *Journal of Lightwave Technology*, vol. 41, no. 18, pp. 5820-5826, 2023.
- [9] Y. Liu *et al.*, "Reconfigurable Microwave Photonic Bandpass Filter Based on CROW," *Journal of Lightwave Technology*, vol. 42, no. 5, pp. 1597-1604, 2024.
- [10] L. Huo *et al.*, "IIR Microwave Photonic Filters Based on Homogeneous Multicore Fibers," *Journal of Lightwave Technology*, vol. 36, no. 19, pp. 4298-4304, 2018.
- [11] J. Liu *et al.*, "Ultrahigh-Q microwave photonic filter with tunable Q value utilizing cascaded optical-electrical feedback loops," *Opt. Lett.*, vol. 38, no. 21, pp. 4304-4307, 2013.
- [12] H. Yan *et al.*, "Wideband-Tunable on-Chip Microwave Photonic Filter with Ultrahigh-Q U-Bend-Mach-Zehnder-Interferometer-Coupled Microring Resonators," *Laser Photon. Rev.*, vol. 17, no. 11, pp. 2300347, 2023.
- [13] L. Liu *et al.*, "Si3N4-Based Narrowband and High Peak Rejection Microwave Photonic Filter With Adjustable Bandwidth," *Journal of Lightwave Technology*, vol. 42, no. 5, pp. 1580-1585, 2024.
- [14] M. Garrett *et al.*, "Integrated microwave photonic notch filter using a heterogeneously integrated Brillouin and active-silicon photonic circuit," *Nat. Commun.*, vol. 14, no. 1, pp. 7544, 2023.
- [15] R. Zhang *et al.*, "Tunable Microwave Photonic Filter with Ultra-Narrow Passband and High Out-of-Band Rejection," *Journal of Lightwave Technology*, pp. 1-8, 2024.
- [16] D. B. Hunter *et al.*, "Tunable optical transversal filter based on chirped gratings," *Electronics Letters*, vol. 31, pp. 1-3, https://digital-library.theiet.org/content/journals/10.1049/el_19951495, 1995.
- [17] Z. Zhu *et al.*, "All-positive-coefficient microwave photonic filter with rectangular response," *Opt. Lett.*, vol. 42, no. 15, pp. 3012-3015, 2017.
- [18] X. Xu *et al.*, "Advanced Adaptive Photonic RF Filters with 80 Taps Based on an Integrated Optical Micro-Comb Source," *Journal of Lightwave Technology*, vol. 37, no. 4, pp. 1288-1295, 2019.
- [19] X. Xu *et al.*, "High performance RF filters via bandwidth scaling with Kerr micro-combs," *APL Photonics*, vol. 4, no. 2, pp. 8, 2019.

- [20] Y. Sun *et al.*, "Applications of optical microcombs," *Adv. Opt. Photon.*, vol. 15, no. 1, pp. 86-175, 2023.
- [21] A. Pasquazi *et al.*, "Micro-combs: A novel generation of optical sources," *Physics Reports*, vol. 729, pp. 1-81, 2018.
- [22] L. Chang *et al.*, "Integrated optical frequency comb technologies," *Nat. Photonics*, vol. 16, no. 2, pp. 95-108, 2022.
- [23] X. Xu *et al.*, "11 TOPS photonic convolutional accelerator for optical neural networks," *Nature*, vol. 589, no. 7840, pp. 44-51, 2021.
- [24] S. Chen *et al.*, "High-Bit-Efficiency TOPS Optical Tensor Convolutional Accelerator Using Microcombs," *Laser Photon. Rev.*, vol. 19, no. 9, pp. 2401975, 2025.
- [25] Y. Bai *et al.*, "TOPS-speed complex-valued convolutional accelerator for feature extraction and inference," *Nat. Commun.*, vol. 16, no. 1, pp. 292, 2025.
- [26] X. Xu *et al.*, "Advanced RF and microwave functions based on an integrated optical frequency comb source," *Opt. Express*, vol. 26, no. 3, pp. 2569-2583, 2018.
- [27] J. Capmany *et al.*, "Discrete-time optical processing of microwave signals," *Journal of Lightwave Technology*, vol. 23, no. 2, pp. 702-723, 2005.
- [28] L. Razzari *et al.*, "CMOS-compatible integrated optical hyper-parametric oscillator," *Nat. Photonics*, vol. 4, no. 1, pp. 41-45, 2010.
- [29] D. Moss *et al.*, "New CMOS-compatible platforms based on silicon nitride and Hydex for nonlinear optics," *Nat. Photonics*, vol. 7, no. 8, pp. 597-607, 2013.
- [30] X. Xu *et al.*, "Photonic Perceptron Based on a Kerr Microcomb for High-Speed, Scalable, Optical Neural Networks," *Laser Photon. Rev.*, vol. 14, no. 10, pp. 10, 2020.
- [31] C. E. Murray *et al.*, "Investigating the thermal robustness of soliton crystal microcombs," *Opt. Express*, vol. 31, no. 23, pp. 37749-37762, 2023.
- [32] W. Wang *et al.*, "Robust soliton crystals in a thermally controlled microresonator," *Opt. Lett.*, vol. 43, no. 9, pp. 2002-2005, 2018.
- [33] B. Corcoran *et al.*, "Ultra-dense optical data transmission over standard fibre with a single chip source," *Nat. Commun.*, vol. 11, no. 1, pp. 7, 2020.
- [34] X. Xu *et al.*, "High performance RF filters via bandwidth scaling with Kerr micro-combs," *APL Photonics*, vol. 4, no. 2, pp. 026102, 2019.
- [35] Y. Li *et al.*, "Performance Analysis of Microwave Photonic Spectral Filters based on Optical Microcombs," *Advanced Physics Research*, vol. 4, no. 1, pp. 2400084, 2025.
- [36] Y. Li *et al.*, "Feedback Control in Microwave Photonic Transversal Filter Systems Based on Optical Microcombs," *IEEE Journal of Selected Topics in Quantum Electronics*, vol. 30, no. 5: Microresonator Frequency Comb Technologies, pp. 1-17, 2024.
- [37] Y. Sun *et al.*, "Optimizing the Accuracy of Microcomb-Based Microwave Photonic Transversal Signal Processors," *Journal of Lightwave Technology*, vol. 41, no. 23, pp. 7223-7237, 2023.
- [38] L. Juseop *et al.*, "A dual-passband filter of canonical structure for satellite applications," *IEEE Microwave and Wireless Components Letters*, vol. 14, no. 6, pp. 271-273, 2004.
- [39] W. S. Chang *et al.*, "Analytical Design of Microstrip Short-Circuit Terminated Stepped-Impedance Resonator Dual-Band Filters," *IEEE Transactions on Microwave Theory and Techniques*, vol. 59, no. 7, pp. 1730-1739, 2011.
- [40] L. Gao *et al.*, "Microwave Photonic Filter With Two Independently Tunable Passbands Using a Phase Modulator and an Equivalent Phase-Shifted Fiber Bragg Grating," *IEEE Transactions on Microwave Theory and Techniques*, vol. 62, no. 2, pp. 380-387, 2014.

- [41] D. Marpaung *et al.*, “Integrated microwave photonics,” *Laser Photon. Rev.*, vol. 7, no. 4, pp. 506-538, 2013.
- [42] V. J. Urick *et al.*, *Fundamentals of microwave photonics*: John Wiley & Sons, 2015.
- [43] M. Garrett *et al.*, “Multi-Band and Frequency-Agile Chip-Based RF Photonic Filter for Ultra-Deep Interference Rejection,” *Journal of Lightwave Technology*, vol. 40, no. 6, pp. 1672-1680, 2022.
- [44] Y. Stern *et al.*, “Tunable sharp and highly selective microwave-photonic band-pass filters based on stimulated Brillouin scattering,” *Photonics Res.*, vol. 2, no. 4, pp. B18-B25, 2014.
- [45] M. Nikles *et al.*, “Brillouin gain spectrum characterization in single-mode optical fibers,” *Journal of Lightwave Technology*, vol. 15, no. 10, pp. 1842-1851, 1997.
- [46] A. Choudhary *et al.*, “Tailoring of the Brillouin gain for on-chip widely tunable and reconfigurable broadband microwave photonic filters,” *Opt. Lett.*, vol. 41, no. 3, pp. 436-439, 2016.
- [47] J. S. Fandiño *et al.*, “A monolithic integrated photonic microwave filter,” *Nat. Photonics*, vol. 11, no. 2, pp. 124-129, 2017.

- 48. L. Razzari, et al., “CMOS-compatible integrated optical hyper-parametric oscillator,” *Nature Photonics*, vol. 4, no. 1, pp. 41-45, 2010.
- 49. D. J. Moss, R. Morandotti, A. L. Gaeta, and M. Lipson, “New CMOS-compatible platforms based on silicon nitride and Hydex for nonlinear optics,” *Nature Photonics*, vol. 7, no. 8, pp. 597-607, 2013/08/01, 2013.
- 50. A. Pasquazi, et al., “Sub-picosecond phase-sensitive optical pulse characterization on a chip”, *Nature Photonics*, vol. 5, no. 10, pp. 618-623 (2011).
- 51. M Ferrera et al., “On-Chip ultra-fast 1st and 2nd order CMOS compatible all-optical integration”, *Optics Express* vol. 19 (23), 23153-23161 (2011).
- 52. Bao, C., et al., Direct soliton generation in microresonators, *Opt. Lett.* 42, 2519 (2017).
- 53. M.Ferrera et al., “CMOS compatible integrated all-optical RF spectrum analyzer”, *Optics Express*, vol. 22, no. 18, 21488 - 21498 (2014).
- 54. M. Kues, et al., “Passively modelocked laser with an ultra-narrow spectral width”, *Nature Photonics*, vol. 11, no. 3, pp. 159, 2017.
- 55. M. Ferrera, et al., “Low-power continuous-wave nonlinear optics in doped silica glass integrated waveguide structures,” *Nature Photonics*, vol. 2, no. 12, pp. 737-740, 2008.
- 56. M.Ferrera et al. “On-Chip ultra-fast 1st and 2nd order CMOS compatible all-optical integration”, *Opt. Express*, vol. 19, (23)pp. 23153-23161 (2011).
- 57. D. Duchesne, M. Peccianti, M. R. E. Lamont, et al., “Supercontinuum generation in a high index doped silica glass spiral waveguide,” *Optics Express*, vol. 18, no. 2, pp. 923-930, 2010.
- 58. H Bao, L Olivieri, M Rowley, ST Chu, BE Little, R Morandotti, DJ Moss, ... “Turing patterns in a fiber laser with a nested microresonator: Robust and controllable microcomb generation”, *Physical Review Research* vol. 2 (2), 023395 (2020).
- 59. M. Ferrera, et al., “On-chip CMOS-compatible all-optical integrator”, *Nature Communications*, vol. 1, Article 29, 2010.
- 60. A. Pasquazi, et al., “All-optical wavelength conversion in an integrated ring resonator,” *Optics Express*, vol. 18, no. 4, pp. 3858-3863, 2010.

61. A.Pasquazi, Y. Park, J. Azana, et al., “Efficient wavelength conversion and net parametric gain via Four Wave Mixing in a high index doped silica waveguide,” *Optics Express*, vol. 18, no. 8, pp. 7634-7641, 2010.
62. Peccianti, M. Ferrera, L. Razzari, et al., “Subpicosecond optical pulse compression via an integrated nonlinear chirper,” *Optics Express*, vol. 18, no. 8, pp. 7625-7633, 2010.
63. M Ferrera, Y Park, L Razzari, BE Little, ST Chu, R Morandotti, DJ Moss, ... et al., “All-optical 1st and 2nd order integration on a chip”, *Optics Express* vol. 19 (23), 23153-23161 (2011).
64. M. Ferrera et al., “Low Power CW Parametric Mixing in a Low Dispersion High Index Doped Silica Glass Micro-Ring Resonator with Q-factor > 1 Million”, *Optics Express*, vol.17, no. 16, pp. 14098–14103 (2009).
65. M. Peccianti, et al., “Demonstration of an ultrafast nonlinear microcavity modelocked laser”, *Nature Communications*, vol. 3, pp. 765, 2012.
66. A.Pasquazi, et al., “Self-locked optical parametric oscillation in a CMOS compatible microring resonator: a route to robust optical frequency comb generation on a chip,” *Optics Express*, vol. 21, no. 11, pp. 13333-13341, 2013.
67. A.Pasquazi, et al., “Stable, dual mode, high repetition rate mode-locked laser based on a microring resonator,” *Optics Express*, vol. 20, no. 24, pp. 27355-27362, 2012.
68. Pasquazi, A. et al., Micro-combs: a novel generation of optical sources. *Physics Reports* 729, 1-81 (2018).
69. H. Bao, et al., Laser cavity-soliton microcombs, *Nature Photonics*, vol. 13, no. 6, pp. 384-389, Jun. 2019.
70. A. Cutrona et al., “High Conversion Efficiency in Laser Cavity-Soliton Microcombs”, *Optics Express* Vol. 30, Issue 22, 39816-39825 (2022). doi.org/10.1364/OE.470376.
71. A. Cutrona et al., “Nonlocal bonding of a soliton and a blue-detuned state in a microcomb laser”, *Nature Communications Physics* **6** Article 259 (2023). [doi:10.1038/s42005-023-01372-0](https://doi.org/10.1038/s42005-023-01372-0).
72. A. A. Rahim et al., “Mode-locked laser with multiple timescales in a microresonator-based nested cavity”, *APL Photonics* **9** 031302 (2024). DOI:10.1063/5.0174697.
73. A. Cooper et al., “Parametric interaction of laser cavity-solitons with an external CW pump”, *Optics Express* **32** (12), 21783-21794 (2024).
74. A. Cutrona et al., “Stability Properties of Laser Cavity-Solitons for Metrological Applications”, *Applied Physics Letters* **122** (12) 121104 (2023). doi: 10.1063/5.0134147.
75. C. E. Murray et al., “Investigating the thermal robustness of soliton crystal microcombs”, *Optics Express* **31**(23), 37749-37762 (2023).
76. Y. Sun et al., “Enhancing laser temperature stability by passive self-injection locking to a micro-ring resonator”, *Optics Express* **32** (13) 23841-23855 (2024). [DOI:10.1364/OE.515269](https://doi.org/10.1364/OE.515269).
77. Y. Sun et al., “Self-locking of free-running DFB lasers to a single microring resonator for dense WDM”, *Journal of Lightwave Technology* **43** (4) 1995-2002 (2025). DOI: 10.1109/JLT.2024.3494694.

78. X. Xu et al., “Reconfigurable broadband microwave photonic intensity differentiator based on an integrated optical frequency comb source,” *APL Photonics*, vol. 2, no. 9, 096104 (2017).
79. Xu, X., et al., Photonic microwave true time delays for phased array antennas using a 49 GHz FSR integrated micro-comb source, *Photonics Research*, vol. 6, B30-B36 (2018).
80. X. Xu, M. Tan, J. Wu, R. Morandotti, A. Mitchell, and D. J. Moss, “Microcomb-based photonic RF signal processing”, *IEEE Photonics Technology Letters*, vol. 31 no. 23 1854-1857, 2019.
81. Xu, et al., “Advanced adaptive photonic RF filters with 80 taps based on an integrated optical micro-comb source,” *Journal of Lightwave Technology*, vol. 37, no. 4, pp. 1288-1295 (2019).
82. X. Xu, et al., “Photonic RF and microwave integrator with soliton crystal microcombs”, *IEEE Transactions on Circuits and Systems II: Express Briefs*, vol. 67, no. 12, pp. 3582-3586, 2020. DOI:10.1109/TCSII.2020.2995682.
83. X. Xu, et al., “High performance RF filters via bandwidth scaling with Kerr micro-combs,” *APL Photonics*, vol. 4 (2) 026102. 2019.
84. M. Tan, et al., “Microwave and RF photonic fractional Hilbert transformer based on a 50 GHz Kerr micro-comb”, *Journal of Lightwave Technology*, vol. 37, no. 24, pp. 6097 – 6104, 2019.
85. M. Tan, et al., “RF and microwave fractional differentiator based on photonics”, *IEEE Transactions on Circuits and Systems: Express Briefs*, vol. 67, no.11, pp. 2767-2771, 2020. DOI:10.1109/TCSII.2020.2965158.
86. M. Tan, et al., “Photonic RF arbitrary waveform generator based on a soliton crystal micro-comb source”, *Journal of Lightwave Technology*, vol. 38, no. 22, pp. 6221-6226 (2020). DOI: 10.1109/JLT.2020.3009655.
87. M. Tan, X. Xu, J. Wu, R. Morandotti, A. Mitchell, and D. J. Moss, “RF and microwave high bandwidth signal processing based on Kerr Micro-combs”, *Advances in Physics X*, VOL. 6, NO. 1, 1838946 (2021). DOI:10.1080/23746149.2020.1838946.
88. X. Xu, et al., “Advanced RF and microwave functions based on an integrated optical frequency comb source,” *Opt. Express*, vol. 26 (3) 2569 (2018).
89. M. Tan, X. Xu, J. Wu, B. Corcoran, A. Boes, T. G. Nguyen, S. T. Chu, B. E. Little, R. Morandotti, A. Lowery, A. Mitchell, and D. J. Moss, “Highly Versatile Broadband RF Photonic Fractional Hilbert Transformer Based on a Kerr Soliton Crystal Microcomb”, *Journal of Lightwave Technology* vol. 39 (24) 7581-7587 (2021).
90. Wu, J. et al. RF Photonics: An Optical Microcombs’ Perspective. *IEEE Journal of Selected Topics in Quantum Electronics* Vol. 24, 6101020, 1-20 (2018).
91. T. G. Nguyen et al., “Integrated frequency comb source-based Hilbert transformer for wideband microwave photonic phase analysis,” *Opt. Express*, vol. 23, no. 17, pp. 22087-22097, Aug. 2015.
92. X. Xu, et al., “Broadband RF channelizer based on an integrated optical frequency Kerr comb source,” *Journal of Lightwave Technology*, vol. 36, no. 19, pp. 4519-4526, 2018.

93. X. Xu, et al., “Continuously tunable orthogonally polarized RF optical single sideband generator based on micro-ring resonators,” *Journal of Optics*, vol. 20, no. 11, 115701. 2018.
94. X. Xu, et al., “Orthogonally polarized RF optical single sideband generation and dual-channel equalization based on an integrated microring resonator,” *Journal of Lightwave Technology*, vol. 36, no. 20, pp. 4808-4818. 2018.
95. X. Xu, et al., “Photonic RF phase-encoded signal generation with a microcomb source”, *J. Lightwave Technology*, vol. 38, no. 7, 1722-1727, 2020.
96. X. Xu, et al., Broadband microwave frequency conversion based on an integrated optical micro-comb source”, *Journal of Lightwave Technology*, vol. 38 no. 2, pp. 332-338, 2020.
97. M. Tan, et al., “Photonic RF and microwave filters based on 49GHz and 200GHz Kerr microcombs”, *Optics Comm.* vol. 465,125563, Feb. 22. 2020.
98. X. Xu, et al., “Broadband photonic RF channelizer with 90 channels based on a soliton crystal microcomb”, *Journal of Lightwave Technology*, Vol. 38, no. 18, pp. 5116 – 5121 (2020). doi: 10.1109/JLT.2020.2997699.
99. M. Tan et al, “Orthogonally polarized Photonic Radio Frequency single sideband generation with integrated micro-ring resonators”, *IOP Journal of Semiconductors*, Vol. 42 (4), 041305 (2021). DOI: 10.1088/1674-4926/42/4/041305.
100. M. Tan et al., “Photonic Radio Frequency Channelizers based on Kerr Optical Micro-combs”, *IOP Journal of Semiconductors* Vol. 42 (4), 041302 (2021). DOI:10.1088/1674-4926/42/4/041302.
101. B. Corcoran, et al., “Ultra-dense optical data transmission over standard fiber with a single chip source”, *Nature Communications*, vol. 11, Article:2568, 2020.
102. X. Xu et al, “Photonic perceptron based on a Kerr microcomb for scalable high speed optical neural networks”, *Laser and Photonics Reviews*, vol. 14, no. 8, 2000070 (2020). DOI: 10.1002/lpor.202000070.
103. X. Xu, et al., “11 TOPs photonic convolutional accelerator for optical neural networks”, *Nature* vol. 589, 44-51 (2021).
104. X. Xu et al., “Neuromorphic computing based on wavelength-division multiplexing”, *IEEE Journal of Selected Topics in Quantum Electronics* **29** (2) 7400112 (2023). DOI:10.1109/JSTQE.2022.3203159.
105. Y. Bai et al., “Photonic multiplexing techniques for neuromorphic computing”, *Nanophotonics* vol. 12 (5): 795–817 (2023). DOI:10.1515/nanoph-2022-0485.
106. C. Prayoonyong et al., “Frequency comb distillation for optical superchannel transmission”, *Journal of Lightwave Technology* vol. 39 (23) 7383-7392 (2021). DOI: 10.1109/JLT.2021.3116614.
107. M. Tan et al., “Integral order photonic RF signal processors based on a soliton crystal micro-comb source”, *IOP Journal of Optics* vol. 23 (11) 125701 (2021). DOI:10.1088/2040-8986/ac2eab.
108. Y. Sun et al., “Optimizing the performance of microcomb based microwave photonic transversal signal processors”, *Journal of Lightwave Technology* vol. 41 (23) 7223-7237 (2023). DOI: 10.1109/JLT.2023.3314526.
109. M. Tan et al., “Photonic signal processor for real-time video image processing based on a

Kerr microcomb”, *Nature Communications Engineering* **2** 94 (2023). DOI:10.1038/s44172-023-00135-7.

110. M. Tan et al., “Photonic RF and microwave filters based on 49GHz and 200GHz Kerr microcombs”, *Optics Communications*, vol. 465, 125563 (2020). doi:10.1016/j.optcom.2020.125563.

111. Y. Sun et al., “Quantifying the Accuracy of Microcomb-based Photonic RF Transversal Signal Processors”, *IEEE Journal of Selected Topics in Quantum Electronics* vol. 29 no. 6, 1-17, 7500317 (2023). 10.1109/JSTQE.2023.3266276.

112. Y. Li et al., “Processing accuracy of microcomb-based microwave photonic signal processors for different input signal waveforms”, *MDPI Photonics* **10**, 10111283 (2023). DOI:10.3390/photonics10111283

113. Y. Sun et al., “Comparison of microcomb-based RF photonic transversal signal processors implemented with discrete components versus integrated chips”, *MDPI Micromachines* **14**, 1794 (2023). <https://doi.org/10.3390/mi14091794>

114. Mengxi Tan, David J. Moss, “The laser trick that could put an ultraprecise optical clock on a chip”, *Nature* **624**, (7991) 256-257 (2023). doi.org/10.1038/d41586-023-03782-0.

115. W. Han et al., “Photonic RF Channelization Based on Microcombs”, *IEEE Journal of Selected Topics in Quantum Electronics* **30** (5) 7600417 (2024). DOI:10.1109/JSTQE.2024.3398419.

116. Y. Li et al., “Feedback control in micro-comb-based microwave photonic transversal filter systems”, *IEEE Journal of Selected Topics in Quantum Electronics* Vol. **30** (5) 2900117 (2024). DOI: 10.1109/JSTQE.2024.3377249.

117. W. Han et al., “Dual-polarization RF Channelizer Based on Microcombs”, *Optics Express* **32**, No. 7, 11281-11295 (2024). DOI: 10.1364/OE.519235.

118. Z. Liu et al., “Advances in Soliton Crystals Microcombs”, *Photonics* Vol. 11, 1164 (2024). <https://doi.org/10.3390/photonics11121164>.

119. C. Mazoukh et al., “Genetic algorithm-enhanced microcomb state generation”, *Nature Communications Physics* Vol. 7, Article: 81 (2024). DOI: [10.1038/s42005-024-01558-0](https://doi.org/10.1038/s42005-024-01558-0).

120. S. Chen et al., “High-bit-efficiency TOPS optical tensor convolutional accelerator using micro-combs”, *Laser & Photonics Reviews* **19** 2401975 (2025). DOI: 10.1002/lpor.202401975

121. W. Han et al., “TOPS-speed complex-valued convolutional accelerator for feature extraction and inference”, *Nature Communications* **16** 292 (2025). DOI: 10.1038/s41467-024-55321-8.

122. Y. Li et al., “Performance analysis of microwave photonic spectral filters based on optical microcombs”, *Advanced Physics Research* **4** (9) 2400084 (2025). DOI:10.1002/apxr.202400084.

123. L. di Lauro et al., “Optimization Methods for Integrated and Programmable Photonics in Next-Generation Classical and Quantum Smart Communication and Signal Processing”, *Advances in Optics and Photonics* Vol. **17** (2) (2025).

124. B. Corcoran et al., “Optical microcombs for ultrahigh-bandwidth communications”, *Nature Photonics* Volume **19** (5) 451 - 462 (2025). DOI: 10.1038/s41566-025-01662-9.

125. Q. Ai et al., “Photonic real-time signal processing”, *Nanophotonics* **29** (2025).
126. X. Xu et al., “Microcomb-enabled parallel self- calibration optical convolution streaming processor”, *Light Science and Applications* (2025).
127. S. Chen et al., “Integrated photonic neural networks”, *npj Nanophotonics* **2**, 28 (2025).
128. A. Aadhi et al., “Scalable Photonic Reservoir for Parallel Machine Learning Applications”, *Nature Communications* **17** (2026).
129. H. Arianfard et al., Sagnac interference in integrated photonics”, *Applied Physics Reviews* **10** (1) 011309 (2023). doi: 10.1063/5.0123236.
130. H. Arianfard et al., “Optical analogs of Rabi splitting in integrated waveguide-coupled resonators”, *Advanced Physics Research* **2** 2200123 (2023). DOI: 10.1002/apxr.202200123.
131. H. Arianfard et al., “Spectral shaping based on optical waveguides with advanced Sagnac loop reflectors”, Paper No. PW22O-OE201-20, SPIE-Opto, Integrated Optics: Devices, Materials, and Technologies XXVI, SPIE Photonics West, San Francisco CA January 22 - 27 (2022). doi: 10.1117/12.2607902
132. H. Arianfard et al., “Spectral Shaping Based on Integrated Coupled Sagnac Loop Reflectors Formed by a Self-Coupled Wire Waveguide”, IEEE Photonics Technology Letters vol. 33 (13) 680-683 (2021). DOI:10.1109/LPT.2021.3088089.
133. H. Arianfard et al., “Three Waveguide Coupled Sagnac Loop Reflectors for Advanced Spectral Engineering”, Journal of Lightwave Technology vol. 39 (11) 3478-3487 (2021). DOI: 10.1109/JLT.2021.3066256.
134. H. Arianfard et al., “Advanced Multi-Functional Integrated Photonic Filters based on Coupled Sagnac Loop Reflectors”, Journal of Lightwave Technology vol. 39 Issue: 5, pp.1400-1408 (2021). DOI:10.1109/JLT.2020.3037559.
135. H. Arianfard et al., “Advanced multi-functional integrated photonic filters based on coupled Sagnac loop reflectors”, Paper 11691-4, PW21O-OE203-44, Silicon Photonics XVI, SPIE Photonics West, San Francisco CA March 6-11 (2021). DOI:10.1117/12.2584020
136. J. Wu et al., “Advanced photonic filters via cascaded Sagnac loop reflector resonators in silicon-on-insulator integrated nanowires”, Applied Physics Letters Photonics vol. 3 046102 (2018). DOI:/10.1063/1.5025833
137. J. Wu et al., “Graphene oxide for photonics, electronics and optoelectronics,” *Nature Reviews Chemistry*, vol. 7, no. 3, pp. 162-183, 2023/03/01, 2023.
138. Y. Zhang et al., “Graphene Oxide for Nonlinear Integrated Photonics,” *Laser & Photonics Reviews*, vol. 17, no. 3, pp. 2200512, 2023/03/01, 2023.
139. J. Hu et al., “2D graphene oxide: a versatile thermo-optic material,” *Advanced Functional Materials*, vol. 34, no. 46, pp. 2406799, 2024.
140. J. Wu et al., “Graphene Oxide for Integrated Photonics and Flat Optics,” *Advanced Materials*, vol. 33, no. 3, pp. 2006415, 2021.
141. Y. Zhang et al., “Enhanced Kerr Nonlinearity and Nonlinear Figure of Merit in Silicon Nanowires Integrated with 2D Graphene Oxide Films,” *ACS Applied Materials & Interfaces*, vol. 12, no. 29, pp. 33094-33103, 2020/07/22, 2020.

142. J. Hu et al., "Integrated waveguide and microring polarizers incorporating 2D reduced graphene oxide", *Opto-Electronic Science* **4** 240032 (2025). DOI: 10.29026/oes.2025.240032

143. D. Jin et al., "Silicon photonic waveguide and microring resonator polarizers incorporating 2D graphene oxide films," *Applied Physics Letters*, vol. 125, no. 5, 2024.

144. H. Arianfard et al., "Sagnac interference in integrated photonics," *Applied Physics Reviews*, vol. 10, no. 1, 2023.

145. D. Jin et al., "Modeling of Complex Integrated Photonic Resonators Using the Scattering Matrix Method," *Photonics*, vol. 11, no. 12, pp. 1107, 2024.

146. J. Wu et al., "Graphene Oxide Waveguide and Micro-Ring Resonator Polarizers," *Laser & Photonics Reviews*, vol. 13, no. 9, pp. 1900056, 2019.

147. J. Hu et al., "Thermo-Optic Response and Optical Bistability of Integrated High-Index Doped Silica Ring Resonators," *Sensors*, vol. 23, no. 24, pp. 9767, 2023.

148. Y. Yang et al., "Enhanced four-wave mixing in graphene oxide coated waveguides", *Applied Physics Letters Photonics* vol. 3 120803 (2018). doi: 10.1063/1.5045509.

149. Wu, J. et al., "Graphene oxide waveguide and micro-ring resonator polarizers", *Laser and Photonics Reviews* Vol. 13, 1900056 (2019).

150. J. Wu et al., "Graphene oxide waveguide polarizers and polarization selective micro-ring resonators", *Laser and Photonics Reviews* vol. 13 (9) 1900056 (2019). DOI:10.1002/lpor.201900056.

151. Wu, J. et al. "2D layered graphene oxide films integrated with micro-ring resonators for enhanced nonlinear optics", *Small* Vol. 16, 1906563 (2020).

152. Y. Qu et al., "Enhanced nonlinear four-wave mixing in silicon nitride waveguides integrated with 2D layered graphene oxide films", *Advanced Optical Materials* vol. 8 (21) 2001048 (2020). DOI: 10.1002/adom.202001048.

153. J. Wu et al., "Enhanced nonlinear four-wave mixing in microring resonators integrated with layered graphene oxide films", *Small* vol. 16 (16) 1906563 (2020). DOI: 10.1002/smll.201906563

154. J. Wu et al., "Graphene oxide waveguide polarizers and polarization selective micro-ring resonators", Paper 11282-29, *SPIE Photonics West*, San Francisco, CA (2020). doi: 10.1117/12.2544584

155. Y. Zhang et al., "Design and optimization of four-wave mixing in microring resonators integrated with 2D graphene oxide films", *Journal of Lightwave Technology* Vol. 39 (20) 6553-6562 (2021). DOI:10.1109/JLT.2021.3101292.

156. Y. Qu et al., "Analysis of four-wave mixing in silicon nitride waveguides integrated with 2D layered graphene oxide films", *Journal of Lightwave Technology* Vol. 39 (9) 2902-2910 (2021). DOI: 10.1109/JLT.2021.3059721.

157. Y. Qu et al., "Graphene oxide for enhanced optical nonlinear performance in CMOS compatible integrated devices", Paper No. 11688-30, PW21O-OE109-36, *2D Photonic Materials and Devices IV*, *SPIE Photonics West*, San Francisco CA (2021). DOI:10.1117/12.2583978

158. Y. Zhang et al., "Optimizing the Kerr nonlinear optical performance of silicon waveguides integrated with 2D graphene oxide films", *Journal of Lightwave Technology* Vol. 39 (14) 4671-4683 (2021). DOI: 10.1109/JLT.2021.3069733.

159. Y. Qu et al., “Photo thermal tuning in GO-coated integrated waveguides”, *Micromachines* Vol. 13 1194 (2022). doi.org/10.3390/mi13081194

160. Zhang Y et al., “Graphene oxide-based waveguides for enhanced self-phase modulation”, *Annals of Mathematics and Physics* Vol. 5 (2) 103-106 (2022). DOI:10.17352/amp.000048

161. Y. Zhang et al., “Enhanced spectral broadening of femtosecond optical pulses in silicon nanowires integrated with 2D graphene oxide films”, *Micromachines* Vol. 13 756 (2022). DOI:10.3390/mi13050756.

162. Y. Zhang et al., “Enhanced supercontinuum generated in SiN waveguides coated with GO films”, *Advanced Materials Technologies* **8** (1) 2201796 (2023). DOI:10.1002/admt.202201796.

163. Y. Zhang et al., “Enhanced self-phase modulation in silicon nitride waveguides integrated with 2D graphene oxide films”, *IEEE Journal of Selected Topics in Quantum Electronics* Vol. 29 (1) 5100413 (2023). DOI: 10.1109/JSTQE.2022.3177385

164. Y. Qu et al., “Integrated optical parametric amplifiers in silicon nitride waveguides incorporated with 2D graphene oxide films”, *Light: Advanced Manufacturing* **4** 39 (2023). [DOI:10.37188/lam.2023.039](https://doi.org/10.37188/lam.2023.039).

165. J. Wu et al., “Novel functionality with 2D graphene oxide films integrated on silicon photonic chips”, *Advanced Materials* Vol. 36 2403659 (2024). DOI: 10.1002/adma.202403659.

166. Di Jin et al., “Silicon photonic waveguide and microring resonator polarizers incorporating 2D graphene oxide films”, *Applied Physics Letters*, Vol. 125, 053101 (2024). doi: 10.1063/5.0221793.

167. Y. Zhang et al., “Advanced optical polarizers based on 2D materials”, *npj Nanophotonics* **1**, 28 (2024). DOI: 10.1038/s44310-024-00028-3.

168. Y. Zhang et al., “Graphene oxide for enhanced nonlinear optics in integrated photonic chips”, Paper 12888-16, Conference OE109, 2D Photonic Materials and Devices VII, Chair(s): Arka Majmdar; Carlos M. Torres Jr.; Hui Deng, SPIE Photonics West, San Francisco CA (2024). Proceedings Volume 12888, 2D Photonic Materials and Devices VII; 1288805 (2024). [DOI:10.1117/12.3005069](https://doi.org/10.1117/12.3005069)

169. Di Jin et al., “Thickness and Wavelength Dependent Nonlinear Optical Absorption in 2D Layered MXene Films”, *Small Science* **4** 2400179 (2024). DOI:10.1002/smse202400179;

170. Y. Zhang et al., J “2D material integrated photonics: towards industrial manufacturing and commercialization”, *Applied Physics Letters Photonics* **10** 000000 (2025); doi: 10.1063/5.0249703.

171. L. Jia, “Third-order optical nonlinearities of 2D materials at telecommunications wavelengths”, *Micromachines*, **14** 307 (2023). <https://doi.org/10.3390/mi14020307>.

172. L. Jia et al., “Fabrication Technologies for the On-Chip Integration of 2D Materials”, *Small: Methods* Vol. 6, 2101435 (2022). DOI:10.1002/smtd.202101435.

173. L. Jia et al., “BiOBr nanoflakes with strong nonlinear optical properties towards hybrid integrated photonic devices”, *Applied Physics Letters Photonics* vol. 4 090802 vol. (2019). DOI: 10.1063/1.5116621

174. L. Jia et al., “Large Third-Order Optical Kerr Nonlinearity in Nanometer-Thick PdSe₂ 2D Dichalcogenide Films: Implications for Nonlinear Photonic Devices”, ACS Applied Nano Materials vol. 3 (7) 6876–6883 (2020). DOI:10.1021/acsnano.0c01239.

175. Kues, M. et al. “Quantum optical microcombs”, Nature Photonics vol. 13, (3) 170-179 (2019). doi:10.1038/s41566-019-0363-0

176. C. Reimer, L. Caspani, M. Clerici, et al., “Integrated frequency comb source of heralded single photons,” Optics Express, vol. 22, no. 6, pp. 6535-6546, 2014.

177. C. Reimer, et al., “Cross-polarized photon-pair generation and bi-chromatically pumped optical parametric oscillation on a chip”, Nature Communications, vol. 6, Article 8236, 2015. DOI: 10.1038/ncomms9236.

178. L. Caspani, C. Reimer, M. Kues, et al., “Multifrequency sources of quantum correlated photon pairs on-chip: a path toward integrated Quantum Frequency Combs,” Nanophotonics, vol. 5, no. 2, pp. 351-362, 2016.

179. C. Reimer et al., “Generation of multiphoton entangled quantum states by means of integrated frequency combs,” Science, vol. 351, no. 6278, pp. 1176-1180, 2016.

180. M. Kues, et al., “On-chip generation of high-dimensional entangled quantum states and their coherent control”, Nature, vol. 546, no. 7660, pp. 622-626, 2017.

181. P. Roztocki et al., “Practical system for the generation of pulsed quantum frequency combs,” Optics Express, vol. 25, no. 16, pp. 18940-18949, 2017.

182. Y. Zhang, et al., “Induced photon correlations through superposition of two four-wave mixing processes in integrated cavities”, Laser and Photonics Reviews, vol. 14, no. 7, pp. 2000128, 2020. DOI: 10.1002/lpor.202000128

183. C. Reimer, et al., “High-dimensional one-way quantum processing implemented on d-level cluster states”, Nature Physics, vol. 15, no.2, pp. 148–153, 2019.

184. P. Roztocki et al., “Complex quantum state generation and coherent control based on integrated frequency combs”, Journal of Lightwave Technology vol. 37 (2) 338-347 (2019).

185. S. Sciara et al., “Generation and Processing of Complex Photon States with Quantum Frequency Combs”, IEEE Photonics Technology Letters vol. 31 (23) 1862-1865 (2019). DOI: 10.1109/LPT.2019.2944564.

186. N. Montaut et al., “Progress in integrated and fiber optics for time-bin based quantum information processing”, Advanced Optical Technologies **14** 1560084 (2025). DOI 10.3389/aot.2025.1560084

187. H. Yu et al., “Exploiting nonlocal correlations for dispersion-resilient quantum communications”, *Physical Review Letters* **134** (2025).

188. S. Sciara et al., “Scalable and effective multilevel entangled photon states: A promising tool to boost quantum technologies”, Nanophotonics vol. 10 (18), 4447–4465 (2021). DOI:10.1515/nanoph-2021-0510.

189. L. Caspani, C. Reimer, M. Kues, et al., “Multifrequency sources of quantum correlated photon pairs on-chip: a path toward integrated Quantum Frequency Combs,” Nanophotonics, vol. 5, no. 2, pp. 351-362, 2016.

190. H. Yu et al., “Quantum key distribution implemented with d-level time-bin entangled photons”, *Nature Communications* **16** 171 (2025). [DOI](https://doi.org/10.1038/s41467-024-55345-0):10.1038/s41467-024-55345-0.